RESEARCH ARTICLE

**ADVANCED
ELECTRONIC
MATERIALS**
Open Access

www.advelectronicmat.de

# Insights into a Defective Potassium Sulfido Cobaltate: Giant Magnetic Exchange Bias, Ionic Conductivity, and Electrical Permittivity

*M. Reza Ghazanfari, Simon Steinberg, Konrad Siemensmeyer, Johannes C. Vrijmoed, Mirko Tallu, Stefanie Dehnen, and Günther Thiele**

The novel potassium sulfido cobaltate, $K_2[Co_3S_4]$ is introduced, with 25% vacancies of the cobalt positions within a layered anionic sublattice. The impedance and dielectric investigations indicate a remarkable ionic conductivity of 21.4 mS cm$^{-1}$ at room temperature, which is in the range of highest ever reported values for potassium-ions, as well as a high electrical permittivity of 2650 at 1 kHz, respectively. Magnetometry results indicate an antiferromagnetic structure with giant intrinsic exchange bias fields of 0.432 and 0.161 T at 3 and 20 K respectively, potentially induced by a combination of the interfacial effect of combined magnetic anionic and nonmagnetic cationic sublattices, as well as partial spin canting. The stability of the exchange bias behavior is confirmed by a training effect of less than 18% upon 10 hysteresis cycles. The semiconductivity of the material is determined, both experimentally and theoretically, with a bandgap energy of 1.68 eV. The findings render this material as a promising candidate for both, active electrode material in potassium-ion batteries, and for spintronic applications.

## 1. Introduction

Lithium-ion batteries are extensively utilized in mobile energy storage devices. Despite their satisfying performance, the scarcity and uneven distribution of lithium reserves of less than 20 ppm in the earth's crust, and the growing demand makes it an unsustainable candidate for future usages.[1] Regarding the

abundancy of sodium and potassium, batteries based on those elements can be considered as an ideal alternative. The standard redox potentials of potassium ions (-2.93 V) and sodium ions (-2.71 V),[2] are comparable with lithium ions (-3.04 V), providing higher energy density and working voltage in potassium-ion batteries in comparison with sodium-based cells.[2] Such differences in standard redox potentials can be translated to a possible higher working voltage in potassium-ion cells compared to that of sodium-ion batteries. Despite potassium's higher atomic mass, potassium-ion batteries can still have a higher energy density due to their higher operating voltage. While the higher atomic mass of potassium might suggest a lower gravimetric energy density, the higher voltage—especially in non-aqueous environments—and potential compatibility with certain electrode materials can result in potassium ion batteries achieving a higher energy density compared to Na-ion or even Li-ion batteries.[2] Accordingly, potassium-ion batteries can be considered as a cost-effective ecofriendly alternative. To overcome the challenges of a generally observed lower ionic mobility and the instability of electrode materials in potassium-based battery cells

M. R. Ghazanfari, G. Thiele
Fachbereich Biologie, Chemie, Pharmazie
Freie Universität Berlin
Fabeckstr. 34-36, 14195 Berlin, Germany
E-mail: guenther.thiele@fu-berlin.de
S. Steinberg
Institut für Anorganische Chemie
RWTH Aachen
Landoltweg 1, 52074 Aachen, Germany

K. Siemensmeyer
Helmholtz-Zentrum Berlin für Materialien und Energie
Hahn-Meitner-Platz 1, 14109 Berlin, Germany
J. C. Vrijmoed
Fachbereich Geowissenschaften
Freie Universität Berlin
Malteserstr. 74-100, 12249 Berlin, Germany
M. Tallu, S. Dehnen
Institute of Nanotechnology (INT)
Karlsruhe Institute of Technology (KIT)
Hermann-von-Helmholtz-Platz 1, 76344 Eggenstein-Leopoldshafen, Germany
G. Thiele
Institut für Anorganische und Analytische Chemie
Albert-Ludwigs-Universität Freiburg
79104 Freiburg, Germany

**ADVANCED
SCIENCE NEWS**

www.advancedsciencenews.com

**ADVANCED
ELECTRONIC
MATERIALS**

www.advelectronicmat.de

during the cycling performances, compounds with layered structures and/or anionic sublattices, such as polyanionic metalates, can ease the insertion of potassium ions between anionic layers and potentially provide more stability and higher conductivity.[3] Cobalt-based compounds are well-known materials for both, positive and negative electrodes due to their high theoretical specific capacities, while cobalt sulfides provide higher capacity in comparison with common electrode materials, such as, Prussian blue analogous.[4,5]

Electronic materials containing cobalt atoms or ions with high magnetic anisotropy and resistivity, are also considered for spintronic applications, in particular for magnetic tunnel junction (MTJ) devices.[6,7] In addition to the elemental combination, the structure of the materials, as well as intrinsic and extrinsic defects can determine the magnetic characteristics. The magnetic exchange bias (EB) is one of those magnetic characteristics for potential spintronic applications including spin valves, single electron transistors, and the next generation of data storage devices, such as, magnetic random access memory (MRAM) sets.[6–10] The exchange bias is a magnetic interfacial phenomenon, theoretically raised from the combination of two different magnetic orders, mostly within thin films of a ferromagnetic (FM) phase coupled in a sandwich structure with an antiferromagnetic (AFM) phase.[8] The origin of exchange bias effects is not fully known so far. In recent years, the interaction of magnetic moments at the interface of the different phases and their impacts to pin the magnetic moments as barriers for their movement was one focus of investigations.[8,9] There are a few reports presenting an intrinsic EB field in single phases such as $LaFeO_3$ and $LaMnO_3$ due to the partial disordering in the AFM parent-structure and the subsequent spin canting effect.[10] This effect is commonly described as a small tilting of spins about their ideal axes to create non-zero magnetic moments in the vicinity of disordered area.[8] The spin canting effect is mostly observed in magnetic nanoparticles, core-shell structures, and antiferromagnetic phases.[8] Relativistic effects of spin-orbit coupling, structural defects inside the compounds, interfaces of nonsimilar phases, and non-bonding surfaces can be considered as the main origins of this effect.[7,8] Although there is no official definition for the range of EB fields, in the literature fields in the range of 20–200 mT are commonly considered "large," 200–1000 mT "gigantic," and for fields larger than 1000 mT "colossal."[8,9] A giant EB field (0.36 T at 5 K) is reported in a single phase of $SrRuO_3$ induced by defects due to the disorder-induced weak localization of magnetic moments in the AFM nature.[9] We recently introduced a large exchange bias field in $K_2[Fe_3S_4]$ with a layered anionic sublattice including a statistical vacancy of iron atoms.[11]

Here, we introduce the synthesis and characterization of a novel ternary compound, $K_2[Co_3S_4]$ (1), with 25% of statistical vacancies of cobalt, including magnetic, dielectric, and ionic conductivity properties. To the best of our knowledge, this work is the first report on the exchange bias and electrical characteristics of the class of ternary chalcogenido cobaltates, while the literature-known compounds of the elemental combination of potassium, cobalt, and sulfur are limited to $K_2[CoS_2]$,[12] $K_9[Co_2S_7]$,[13] and $K_6[CoS_4]$.[14]

$$K_2S + 3\,CoS \xrightarrow[\approx 10\ \text{min}]{\approx 1300\ \text{K}} K_2[Co_3S_4]$$

**Scheme 1.** Reaction equation of the synthetic process towards **1** by means of solid-state reaction starting from a stoichiometric ratio of $K_2S$ and $CoS$.

## 2. Results and Discussion

### 2.1. Synthesis and Structural Characteristics

**1** was obtained through a straightforward solid-state technique by fusion of the binary precursors $K_2S$ and $CoS$ at approximately 1300 K for 10 min. **Scheme 1** displays the equation of the reaction towards **1**. The reaction is almost quantitative (93% yield, loss due to adhering product to the reaction container) and can be scaled up to 50 g per batch, limited only by the volume of the reaction container. The as-synthesized dark green powder obtains a metallic shining appearance.

Single crystals of **1**, obtained through a solvothermal treatment, display a plate-shape morphology with a dark turquoise color. **1** crystalizes in the tetragonal space group type $I4/mmm$. **Figure 1** shows a depiction of the crystal structure of **1**. Cobalt ions are coordinated by sulfur ions to yield $[CoS_4]^{6-}$ tetrahedra. Those tetrahedra are edge-sharing to yield a 2D anionic sublattice. Potassium ions are positioned between anionic layers. Crystallographic investigations reveal the statistically occupation of cobalt positions of 75%. Thus, **1** is isotypic to $K_2[Fe_3S_4]$,[11] a defect-variant of $K_2[Fe_4Se_4]$ structure type.[15] Detailed information on the refinement results as well as the structural parameters such as ion positions, bond length, and bond angles are provided in the Supporting Information. **1** has smaller cavities comprising the cobalt vacancies in the anionic layers (d(S–S) = 3.75(4)–3.76(6) Å) compared to the iron vacancies in $K_2[Fe_3S_4]$ (d(S–S) = 3.77(8)–3.85(6) Å) due to the smaller ionic radius of $Co^{2+}$ (0.72 Å) compared to $Fe^{2+}$ (0.77 Å). The distance of the anionic layers in **1** (d(S–S) in two parallel anionic layers: 3.97 Å) is—despite the smaller atomic radii of cobalt ions—slightly longer compared to that of the isotypic iron compound (3.89 Å). **1** is the first potassium sulfido cobaltate with a 2D interconnection of the anionic sublattice, which warrants electronic and magnetic investigations. The purity of the obtained powder was evaluated using powder X-ray diffraction analysis (XRD) and Rietveld refinement, which confirms the presence of **1** with very low amount (<3 wt%) of potassium (di)sulfide, $K_2S$ and $K_2S_2$, as impurities (**Figure 2a**) and indicates an average crystallite size of 398 ± 12 nm and a crystallinity degree of 93% ± 2%. In Figure 2a, the small reflexes belonging to the impurities are highlighted. However, due to their very low intensity (comparable to the background noise), precise determination of the quantity is not very accurate by means of Rietveld refinement. Considering the small percentage of these phases, as well as their diamagnetic natures, an impact on the magnetic properties is not very likely. More details of the XRD analysis and the Rietveld refinement are available in the Supporting Information. Figure 2b shows the results of energy dispersive X-ray (EDX) measurements, verifying the elemental

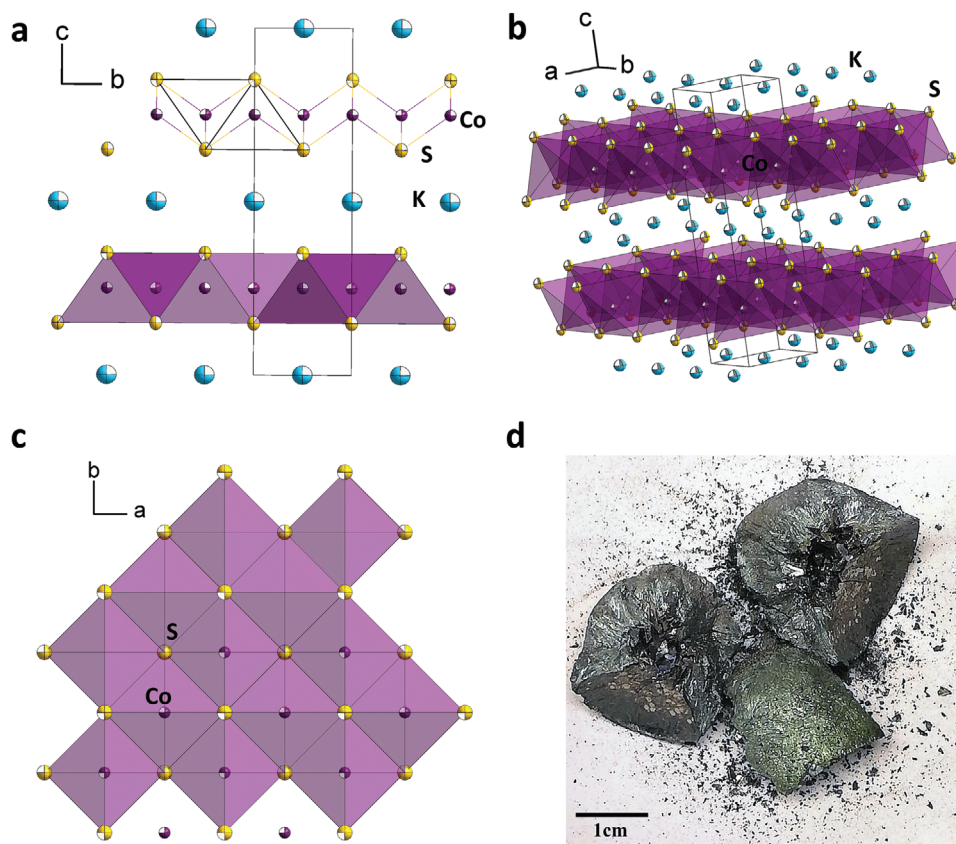**ADVANCED
SCIENCE NEWS**

www.advancedsciencenews.com

**ADVANCED
ELECTRONIC
MATERIALS**
Open Access

www.advelectronicmat.de

**Figure 1.** Excerpt from the crystal structure of **1**. a) Depicted along *a* including edge-sharing $[CoS_4]^{6-}$-tetrahedra. b) 2D anionic substructure of $[Co_3S_4]^{2-}$ as layers in the *ab* plane. c) Depicted along *a* including edge-sharing $[CoS_4]^{6-}$-tetrahedra. d) Appearance of the **1** after solid-state reaction, displaying the dark green color of the bulk material. Selected bond lengths and angles: Co—S: 2.2911(12) Å, K—S: 3.2826(13) Å, S—Co—S: 109.28(4)−109.85(9)°. Partial occupation of cobalt atoms is omitted for clarity.

composition of **1** according to the nominal stoichiometric ratio of 2:3:4 for K:Co:S.

Thermogravimetric (TG) results (Figure S1, Supporting Information) indicate a negligible weight loss up to 1000 K. Subsequent heating up to 1200 K results in a weight loss of approximately 3%, indicating a remarkable thermal stability. Small endothermic signals in the differential scanning calorimetry (DSC) curves at around 700 K suggest a high-temperature phase transition but are not associated with the compound's melting point according to our synthetic observations. An additional endothermic signal around 950 K observed only in the first heating cycle of the DSC might be attributed to impurities that are invisible in the powder XRD and EDX or an additional, irreversible phase transition. However, powder XRD analysis of **1** after heat treatment at 1200 K for 12 h does not indicate any structural changes of the bulk material.

### 2.2. Magnetic Properties

To reveal the main magnetic ordering of **1**, susceptibility measurements were carried out. The inverse of magnetic susceptibility curve versus temperature is displayed in **Figure 3**a, indicating a deviation from the fitting line of the Curie-Weiss law. The negative value of the Curie-Weiss constant of around -780 K is evidence of the AFM structure of **1**.[16] The high absolute value of the Curie-Weiss constant proves the strong AFM interaction within the compound. The starting point of the non-compliance (separation point of the inverse susceptibility curve and Curie-Weiss fitted line) shows a Néel temperature of around 200 K, as a transition temperature to paramagnetic behavior. The magnetization curves as a function of external applied field up to 4.00 T (Figure 3b) indicate the hysteresis curves at low temperatures of 3, 20, and 100 K, while the increase of the temperature changes the curves to narrower loops, decreasing the coercivity and remanent magnetization values. At these temperatures, the plots show a linear trend upon the applied field of higher than 0.35 T, which could be considered as another indication of an AFM structure. At a temperature of 300 K, the curve shows a fully linear trend of magnetization plot as evidence of the paramagnetic structure, which agrees with the derived Néel temperature of around 200 K in the inverse susceptibility curve (Figure 3a). At low temperatures, the centers of the hysteresis loops (Figure 3b) are shifted from the origin at zero, which is considered a sign of the exchange bias (EB) effect.

The temperature-dependent magnetization curves consisting of the FC and ZFC measurements' results are illustrated in Figure 3c. ZFC and FC curves indicate four transition
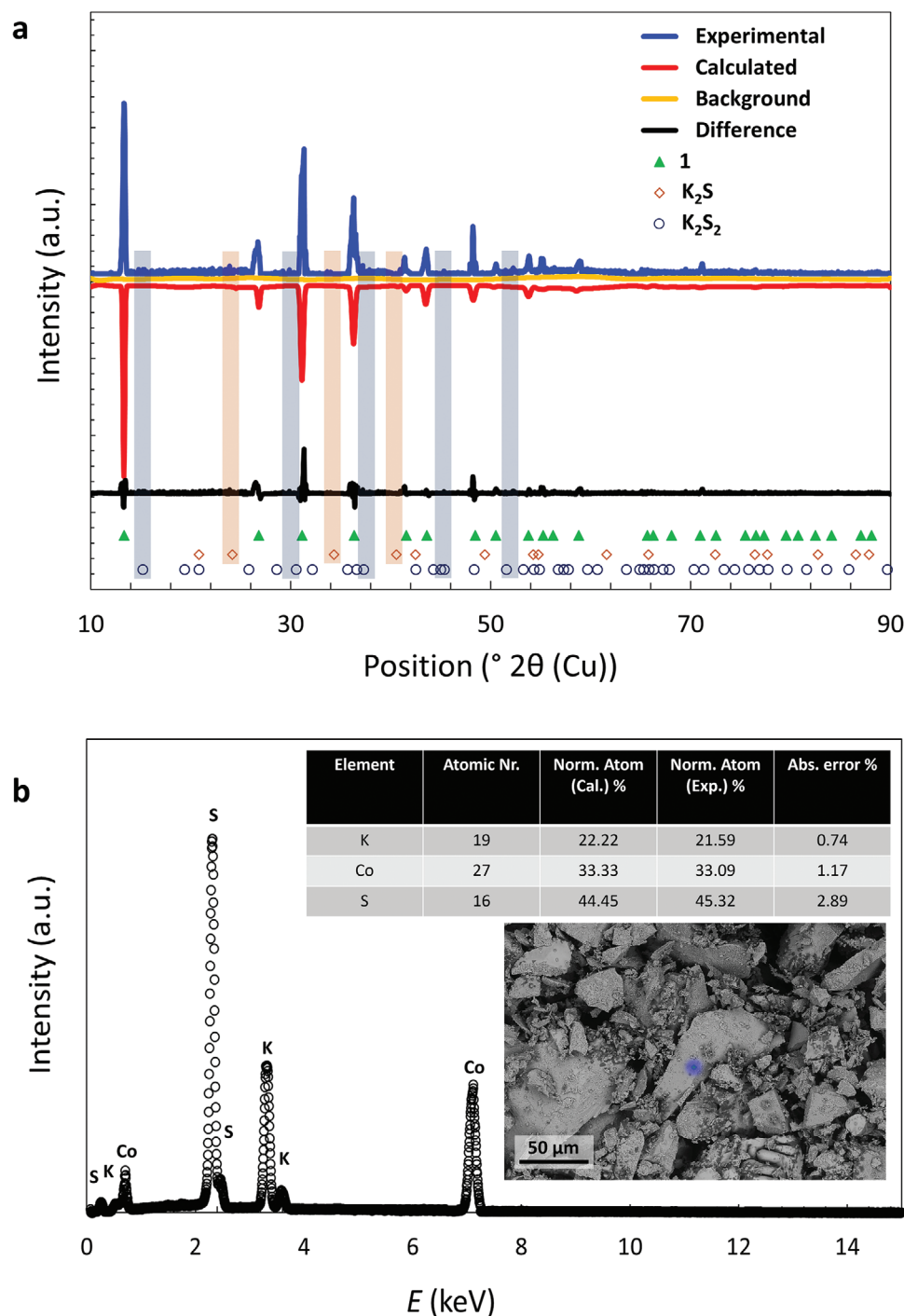
**Figure 2.** a) Rietveld refinement results of as-synthesized **1**, indicating the reflexes belong to **1** as well as side products of potassium (di)sulfide. b) EDX spectrum of powder of **1** based on the point measurements, with the extracted amounts of the elemental ratio according to the average of three different point measurements, and a micrograph of the powder from backscattered electron signals at an applied beam energy of 20 kV using scanning electron microscopy.

points including the Néel temperature at 200 K, the irreversible bifurcation temperature ($T_{Irr}$) at around 65 K, and two anomalies at around 35 and 105 K, which are abbreviated as $T_1$ and $T_2$, respectively. At temperatures lower than $T_{Irr}$, the magnetization is increased, where a spin canting in the AFM structure could be considered as one of the possible origins.[17,18]

Figure 3d demonstrates the close-up view of the field-dependent magnetizations curves, indicating the measured values of the exchange bias field (EBF) at different temperatures. A
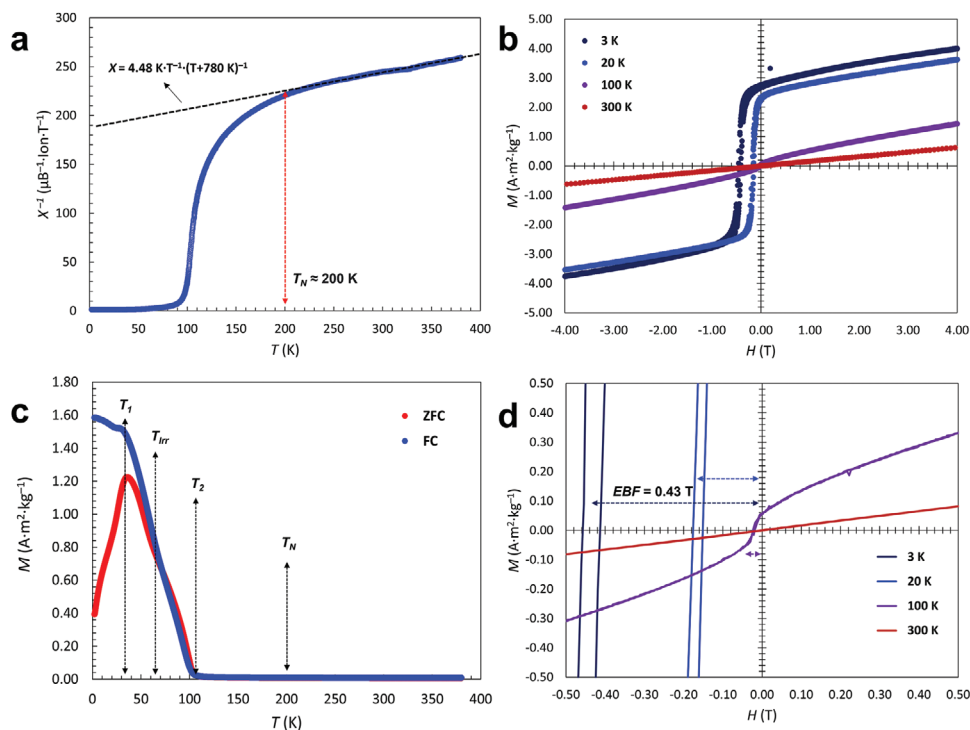
ADVANCED
SCIENCE NEWS

www.advancedsciencenews.com

ADVANCED
ELECTRONIC
MATERIALS
Open Access

www.advelectronicmat.de

**Figure 3.** a) Inverse susceptibility curve (in blue) as a function of the temperature rising with the fitted line (in black) of the Curie-Weiss law. b) Field-dependent magnetization curves for **1** at different temperatures as a function of the external applied field up to 4.00 T. c) Zero field cooling (ZFC) and field cooling (FC) plots of **1** as a function of the measurement temperature, under an applied field of 50 mT, indicating four transition points. d) Close-up view of field-dependent magnetization curves, indicating the observed exchange bias fields.

giant EBF value of around 430 mT is observed at a temperature of 3 K, and as a function of temperature, reduced to 161 mT at 20 K, and 21 mT at 100 K, while the paramagnetic curve at 300 K shows no EBF. Considering the AFM nature of the structure as well as the nonlinear hysteresis of the magnetization curves at the temperatures lower than 200 K, the observed EB effects might be caused by the coexistence of the AFM ordered structure and disordered areas. These areas potentially originate from intrinsic or extrinsic defects that are non-detectable via XRD.[11] Moreover, the magnetic and nonmagnetic characteristics of the anionic sub-lattices (based on the connected $[CoS_4]$ polyhedra) and potassium layers, respectively, might introduce another possible explanation for the observed EBF. These consequent magnetic-nonmagnetic layers could interfacially interact together, leading to make an EB phenomenon. The internal interface between these sublattices can potentially act as bilayers in the conventional definition of EB structures.[8,9] The negligible impurities of potassium poly-sulfides with diamagnetic behavior as well as undetected magnetic phases by PXRD such as CoS might have minor contributions in the observed magnetic phenomena. To exactly determine their potential impacts, further investigations on the atomic and microscopic levels are planned. As another possible reason, the generation of a geometrical magnetic frustration phenomenon and a subsequent localized spin glass phase was already reported as a possible result of structural defects in several materials.[19] The magnetic ion vacancies can demonstrate a deviation from the ideal AFM ordering, defined as the spin canting concept, and result in the formation of weak ferromagnetically coupled clusters.[20] Thus, a spin glass behavior might occur at the inter-face of AFM and those ferromagnetic areas.[20] The simultaneous AFM and potentially induced spin glass phases can be considered as an ordered/disordered magnetic coupling and results in the EB effects.[21] The obtained value is a dramatic increase when compared to the literature reported values of 35 mT for the iso-typic $K_2[Fe_3S_4]$, raised from the potential combination of AFM and spin glass phases.[11] The observed EBF in **1** is an order of magnitude higher than that of $K_2[Fe_3S_4]$, which could originate from the higher magnetocrystalline anisotropy of cobalt-ions.[7,22]

According to the observed behaviors in the field- and temperature-dependent magnetometry measurements (Figure 3b,c), the transition at 105 K could be considered as the transition temperature of the assumed internal spin glass phase, while the EBF vanishes at higher temperatures. $T_1$ at around 35 K might be attributed to weak antiferromagnetic interactions in the anionic layers through a Co–S–Co super-exchange, which was reported for Mn–O–Mn interactions in $LuMnO_3$ as an AFM phase showing a transition above the Néel temperature due to the magnetic disorder.[17] The statistical cobalt vacancies could increase the probability of geometrical distortion in the structure and therefor of the super-exchange interaction between non-neighboring cobalt ions in the *ab* plane with a Co–Co distance of 5.9377(16) Å.

**Figure 4a** indicates the temperature-dependent variation of EBF and coercivity values of the sample. Coercivity values are de-creased from 49 mT at 3 K, to 46 mT at 20, 1.4 at 100 K, and finally fully vanished at 200 K, which are in agreement with the phase
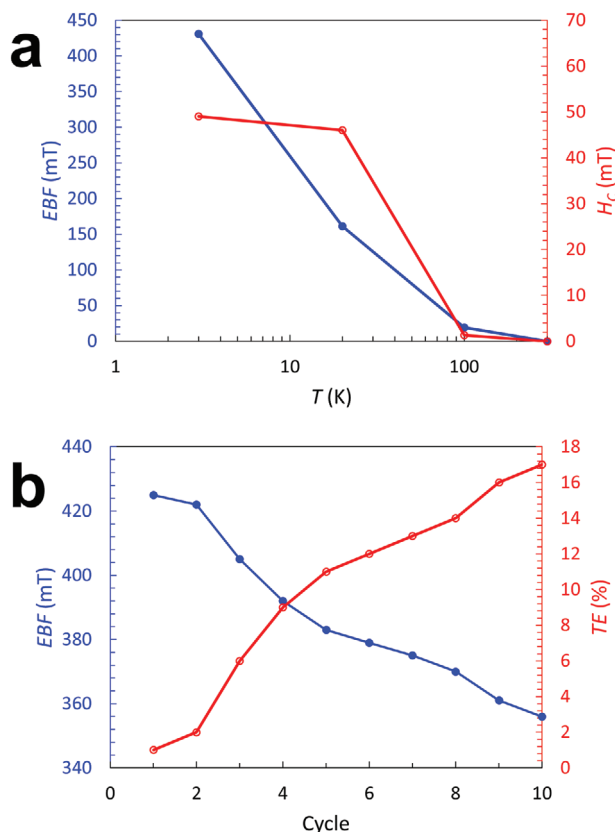
**ADVANCED
SCIENCE NEWS**

www.advancedsciencenews.com

**ADVANCED
ELECTRONIC
MATERIALS**

www.advelectronicmat.de

**Figure 4.** a) Variations of the magnetic exchange bias field, EBF, (left axis, in blue) and magnetic coercivity, $H_C$, (right axis, in red) of **1** as a function of the temperature. b) Variation curves of EBF (left axis, in blue) and calculated training effect, TE, (right axis, in red) of **1** as a function of the hysteresis cycle at 3 K under applied fields up to 4.00 T. Uncertainly errors of 2% (combination of the SQUID calibration and mass determination) should be considered for the absolute values.

transition from AFM, dominant at low temperatures, to a paramagnetic structure at room temperature. Errors of the magnetization measurement arise from uncertainties in the superconducting quantum interference device magnetometer (SQUID) calibration ($\approx$1%) and the mass determination (due to the difference between mass of filled and empty measurement capsule) with similar error (200 mg capsule, typically 10 to 20 mg sample). In conventional EB materials, the interfacial interaction of magnetic-nonmagnetic bilayers leads to an increase of the coercivity field in parallel to an increase in the EBF, where the coercivity values are typically larger than those of the EBF. The absolute values and their relative ratio of the coercivity and the EBF depend on different parameters, such as, the magnetic structures and the thickness and microstructure of the layers. Coercivity values that are smaller than those of the EBF are also frequently reported in literature, particularly in manganese and nickel containing alloys and compounds, such as, FeMn, PtMn, MnN, and NiO.[23,24] To investigate the stability of the EB effect during cyclic hysteresis loops, the training effect parameters were calculated based on the following equation[11,25]:

$$ TE = 100 - \left[ \left( 1 - \left[ (EBF_1 - EBF_n) \cdot EBF_1^{-1} \right] \right) \times 100 \right] \% \qquad (1) $$
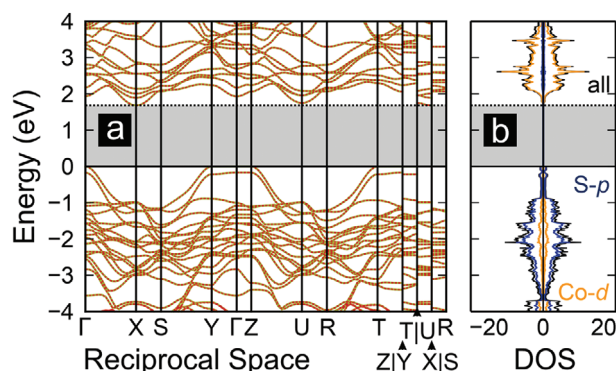


**Figure 5.** a) Calculated spin-resolved electronic band structure of **1**. b) Calculated density of states (DOS) of **1**, including total (all) and elemental-resolved DOS plots.

where TE is training effect, $EBF_1$ is the initially measured exchange bias field, and $EBF_n$ is the observed bias field during $n^{th}$ cycle of the hysteresis loop. Figure 4b displays the variation of the EBF during cyclic hysteresis loops as well as the subsequent TE values at 3 K, showing the bias field reducing from 430 mT to around 360 mT and a TE value of approx. 18% upon ten hysteresis cycles. The comparably small TE value could be vindicated by the high magnetocrystalline anisotropy of the compound, as well as the presence of a spin glass phase.[25–27] Due to complexity of the structure, to prove the exact magnetic structure and behaviors, further investigations, such as neutron powder diffraction and element-specific X-ray absorption near edge analysis will be performed in the future.

### 2.3. Optical and Electrical Properties

To determine the optical properties of **1**, UV–Visible spectroscopy measurements were conducted. The Tauc plot calculated based on the Kubelka-Munk function[28] demonstrates an optical bandgap of around 1.68 eV indicating a semiconductive behavior of **1** (see Figure S2, Supporting Information). The Tauc plot for the indirect transition is almost linear (Figure S3, Supporting Information) without any intersection with the abscissa, which points towards a direct nature of the band gap in **1**. **Figure 5a** displays the electronic spin-resolved band structure of **1** computed by DFT methods, which is based on the obtained optical band gap (vide infra). The contribution of spin-up and spin-down are entirely symmetric according to the AFM structures. The density of states (DOS) plots of cobalt and sulfur contributions as well as total density of states (t-DOS) of **1** are shown in Figure 5b. The plots indicate the main contributions of Co-d and S-p, mainly in the conductive and valence bands, respectively, while the K-s states are mainly located about the conduction band minimum. This outcome indicates that the potassium atoms are oxidized as one-electron donors within ionic K−S bonds, while further analysis of the bond peculiarities will be part of future research.

**Figure 6a** displays the results of dielectric measurements at room temperature, of samples sintered at three different temperatures, i.e., 903, 1003, or 1103 K which are abbreviated as samples **1**-903, **1**-1003, and **1**-1103, respectively. At 1 kHz, as an accepted standard frequency, the dielectric constants ($\kappa$) of **1**-903,

**ADVANCED
SCIENCE NEWS**

www.advancedsciencenews.com

**ADVANCED
ELECTRONIC
MATERIALS**
Open Access

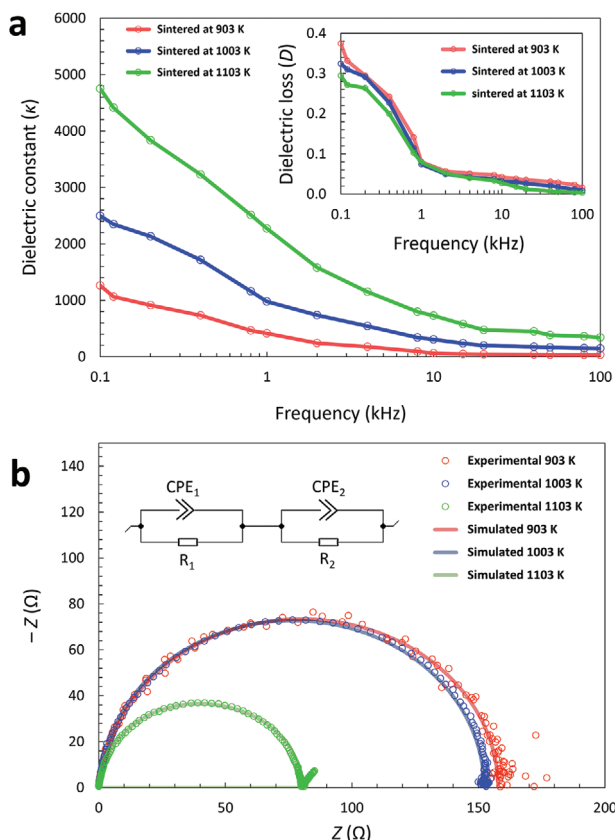www.advelectronicmat.de

**Figure 6.** a) Plot of the dielectric constant of **1**-903, **1**-1003, and **1**-1103 as a function of the measurement frequency. Inset: Plot of the dielectric loss as a function of the measurement frequency. b) Nyquist plot of **1**-903, **1**-1003, and **1**-1103 as well as the simulated complex impedance curves based on a designed equivalent circuit comprising two parallel sets of resistance (*R*) and constant phase element (*CPE*) elements in series (Inset frame).

**1**-1003, and **1**-1103 are around 550, 1220, and 2650, respectively. These values, particularly the one obtained for pellets sintered at the highest possible temperature, are significantly higher than reported values for benchmark dielectric materials for applications as circuit capacitors, such as barium and strontium titanates ($\approx$ 1000 to 2000)[29] as well as high-$\kappa$ dielectric gate standard material ($SiO_2$, $\approx$ 3.9) for the MOSFET applications.[30] The enhanced values of dielectric constants as a function of sintering temperature can be explained by higher densities as well as larger domain to domain boundary ratio which potentially create larger space charge polarization areas.[31] For all samples, an increase of the frequency result in a decrease of the dielectric constant values, sharply in the initial range from 0.1 to 2 kHz, and then gradually in the range of 4 to 100 kHz. As a well-stablished phenomenon, the sharp decreasing is attributed to the vanishing of space charge polarization mechanisms at high frequencies, while it is the dominant mechanism at frequencies lower than 10 kHz.[31] In parallel, the dielectric loss values of all samples are decreased by increasing the frequency. At a frequency of 1 kHz, for all samples these values are lower than 0.1, as a standard criterion of the dielectric loss for capacitor and MOSFET applications, indicating the reliability of the measurements. The increase in sintering

temperature leads to a slight decrease of the loss values due to the higher density of samples sintered at higher temperatures.[32]

The Nyquist plots of the conducted impedance measurements at room temperature of samples sintered at different temperatures as well as the simulated complex impedance plots are shown in Figure 6b. All measurements depict the semi-circular arcs with the intercept points with the real impedance (*Z*) axis at around 159 Ω for **1**-903, 151 Ω for **1**-1003, and 79 Ω for **1**-1103. The corresponding ionic conductivity values calculated based on the Nyquist equation[33] are 9.6, 11.2, and 21.4 mS $cm^{-1}$ for the samples of **1**-903, **1**-1003, and **1**-1103, respectively. To the best of our knowledge, the obtained conductivity value of 21.4 mS $cm^{-1}$ for **1**-1103 is in the range of highest ever reported values for potassium ion conductive materials,[34] and in the same range as found for isotypic $K_2[Fe_3S_4]$ (24.37 mS $cm^{-1}$), which indicates a predominant influence of the structure type on the conductivity.[11] The increase in the sintering temperatures leads to a decrease of the measured impedance values and an enhancement of the calculated ionic conductivity values. These variations can be explained based on the grain–grain boundary model[35] by increasing the ratio of grains to grain boundaries as well as possible effects of higher bulk densities in the samples sintered at higher temperatures due to the adverse impact of porosities on the ionic mobility.[36] In **1**-1103, the impedance plot shows a small tail in the range of low frequencies as an indication of purely ionic conductivity,[37] while for **1**-903 and **1**-1003 the experimental results at low frequencies are noisy and there is no clear tails after the semicircular arcs in the impedance plots. To simulate the Nyquist plots according to the experimental results, an equivalent circuit is defined comprising two parallel sets of resistance (*R*) and constant phase element (*CPE*) elements in series. The *CPE* is used to account for non-ideal capacitive behavior often due to surface roughness, porosity, or heterogeneous reaction kinetics.[38] A pure capacitor would result in a perfect semicircle, but the presence of *CPE* modifies the semicircle shape slightly. The position and shape of the semicircle can provide insights into the impedance characteristics, including charge transfer resistance and the non-ideal capacitive behavior introduced by the *CPE*s.[38] Typically, the Nyquist plot for ionic conductors exhibits a semicircular arc followed by a straight line, representing different impedance contributions. However, if there is only the semicircular arc without a clear tail, it suggests certain conditions or phenomena affecting the impedance response. First possible scenario is based on the grain boundary effects dominated by bulk properties. If the grains themselves are highly conductive and the grain boundaries are not significantly impeding the ion flow, the impedance will be dominated by the bulk properties. This results in a prominent semicircular arc without a noticeable low-frequency tail.[39] Another potential process is the high grain conductivity with negligible grain boundary resistance, while the impedance response primarily reflects the grain contribution. Additionally, if the electrodes used in the measurement have excellent contact and negligible polarization resistance, the low-frequency tail might not be visible.[39] To further analyze and confirm these scenarios, impedance measurements at different temperatures as well as investigations to determine the microstructure will be performed in future studies.

To verify the identity of the analyzed samples after the sintering process and measurements as well as the effects of possible silver

diffusion into the pellets during the heat treatments, the sample of **1**-1103 was investigated by PXRD (Figure S4, Supporting Information). The result confirms the purity of **1** after sintering and measurements.

## 3. Summary and Conclusions

In the present work, $K_2[Co_3S_4]$, as the first layered potassium sulfido cobaltate, was successfully synthesized as single crystals and on a large-scale in bulk through a straightforward and high-yielding technique. The structural investigations display layered anionic sublattices including 25% cobalt vacancies. Sintered samples indicate a high dielectric constant of 2650 at 1 kHz at room temperature, comparable with benchmark dielectric materials, as well as an outstanding ionic conductivity value of 21.4 mS cm$^{-1}$ at room temperature, which is in the range of highest ever reported values for potassium-containing compounds. The variation of the sintering temperature can significantly manipulate the dielectric and ionic mobility characteristics. The magnetometry results demonstrate a giant exchange bias field of around 430 mT, possibly originating from a combination of antiferromagnetic ordering in the presence of spin glass phases. The comparison of the results with the isotypic $K_2[Fe_3S_4]$ indicates potential impacts of electronic and geometric factors on the physical properties. The combination of electrical and magnetic properties, as well as an energy-efficient synthetic method, renders $K_2[Co_3S_4]$ a promising candidate for electrode active materials in battery applications, magnetic materials in spintronics, and multifunctional quantum material.

## 4. Experimental Section

*General Procedure and Materials*: Potassium (Acros Organics, 98%), sulfur (abcr, 99%), and cobalt sulfide (Sigma-Aldrich, 99.5%) were commercially purchased and utilized without any further purification. Potassium sulfide ($K_2S$) was synthesized in liquid ammonia according to the reported procedure.[40] Regarding the sensitivity of the precursors ($K_2S$) and **1** to air and moisture, all synthetic processes, post-processing, and characterizations were conducted under an inert atmosphere using standard Schlenk techniques or gloveboxes with argon atmosphere ($O_2$ and $H_2O$ amounts < 0.1 ppm).

*Synthesis of 1, Bulk and Single Crystal*: Stoichiometric amounts of $K_2S$ (1 eq. 0.05 mol, 5.513 g) and CoS (3 eq., 0.15 mol, 13.648 g) were thoroughly mixed and placed in a silica glass ampule, fused at approximately 1300 K for 10 min with an oxygen-methane hand torch, and allowed to cool down to room temperature. After removing the crude product from the ampule, the obtained regulus is ground to yield 17.75 g (93%) of dark green powder with metallic shining appearance. Single crystals are prepared by solvothermal treatment of 0.125 g of as-synthesized powder in 2 mL ethylenediamine in a 10-mL glass vial at 423 K for 48 h.

*Experimental Characterizations*: Single crystals were isolated and selected under a light microscope, mounted in Paraton oil, and investigated using a Bruker D8 Venture diffractometer with Mo-K$_\alpha$ radiation ($\lambda$ = 0.71073 Å) at 100 K. The structure was solved and refined in Olex 2[41] using ShelXT[42] and ShelXL,[43] respectively, and depicted using DIAMOND4.5.2.[44] The purity of the powder was evaluated using powder XRD, by placing approx. 50 mg powder on a self-printed sample-holder based on the reported protocol,[45] on a Malvern Panalytical Empyrean using Cu-K$_\alpha$ radiation ($\lambda$ = 1.54184 Å) at 293 K. The crystallographic

parameters such as crystallite size and crystallinity degree were calculated according to Rietveld structure refinement[46] using GSAS II.[47] Purity and elemental ratio were evaluated using EDX analysis according to the average of three different point measurements. The obtained structural details, the procedure of the Rietveld refinements, and details of EDX measurements are provided in the Supporting Information.

Samples for magnetometry were prepared by placing approximately 20 mg of fine powder into polyethylene (PE) sample holders and measured at different temperatures including 3, 20, 100, and 300 K under an applied magnetic field of up to 4.00 T using a SQUID (MPMS3-7T Quantum Design). The PE holders are in a capsule form with two parts, while during the sample preparation, the powder is placed in one part and manually pressed between two joint parts to properly affix samples. Temperature-dependent investigations consisting of the zero-field cooled (ZFC) and field cooled (FC) measurements were performed under an applied field of 50 mT. The DC measurements of the susceptibility were conducted under a field of up to 4.00 T, and the Curie-Weiss law was fitted to the inverse susceptibility curve. Further details of magnetometry measurements are provided in the Supporting Information. To study the dielectric and impedance properties, the bulk samples were prepared by pressing fine power of **1** as pellets and sintering at temperatures of 903, 1003, or 1103 K for 12 h. After adding a conductive silver paste (abcr, sheet resistivity < 3.8 × 10$^{-3}$ Ω cm$^{-1}$, for the layer thickness of 3.8 × 10$^{-4}$ cm) as electrodes to both sides of the sintered pellets, the dielectric parameters including capacitance, dielectric constant, and dielectric loss were acquired as a function of the applied frequency in the range of 0.1 to 100 kHz at room temperature using a LCR meter (East Tester, ET4410). Further information regarding the sample preparations, measurements, and calculations of dielectric constants are available in the Supporting Information. The impedance parameters including real part (Z) and imaginary part (Z') of impedance of the sintered samples were measured at room temperature in the frequency range of 100 mHz to 1 MHz with a resolution voltage of 50 µV using an electrochemical impedance analyzer (EIS, BioLogic MTZ-35). The Nyquist equation and plot were employed to calculate the ionic conductivity values of the samples,[33] while the simulation of complex impedance plots was carried out based on a designed equivalent circuit in ZSimpWin program.[48] The optical bandgap of **1** was calculated according to a Tauc plot obtained from the results of UV–visible spectroscopy (for more details see the Supporting Information).

*Quantum Chemical (DFT) Calculations*: All spin-polarized electronic structure computations were accomplished using the projector augmented wave method[49] (PAW) as implemented in the Vienna ab initio simulation package (VASP).[26,49,50,51] Prior to the analysis of the electronic structure, full optimizations including lattice parameters and atomic positions were completed for a model approximating the crystal structure of $K_2[Co_3S_4]$ (Figure S5, Supporting Information). Correlation and exchange in all computations were described by the generalized gradient approximation (GGA) with the Perdew-Burke-Ernzerhof (PBE) exchange correlation functional;[52] Yet, this type of functional failed to describe the strong correlations related to the electrons within the Co-3d atomic orbitals. To describe these strong correlations, a Hubbard correction parameter ($U_{eff}$ = 8.5 eV) was included in full accordance with more recent research[11] on this particular family of compounds. In addition to these corrections, the influence of dispersive interactions whose nature is typically underestimated by the aforementioned sort of functional was also probed by introducing a van-der-Waals dispersion interaction term.[27,53] The energy cut-off of the plane wave basis set was 500 eV in all computations, while a set of 7 × 14 × 4 k-points was used to sample the first Brillouin zone (note that the k-points set differs from that expected for a tetragonal symmetry due to the employed starting model). All computations were considered to be converged, as the energy differences between two iterative steps fell below 10$^{-8}$ and 10$^{-6}$ eV of the electronic and ionic relaxations, respectively. The coordinates of the high-symmetry **k**-paths in the Brillouin zone were generated using AFLOW,[54] while the electronic band structure and DOS were analyzed as well as plotted using the pymatgen[55] and wxDragon[56] codes, respectively.

**ADVANCED
SCIENCE NEWS**

www.advancedsciencenews.com

**ADVANCED
ELECTRONIC
MATERIALS**
Open Access

www.advelectronicmat.de

## Supporting Information

## Acknowledgements

## Conflict of Interest

The authors declare no conflict of interest.

## Author Contributions

Conceptualization: M.R.G., G.T.; project administration: M.R.G., G.T.; Writing initial draft: M.R.G.; formal analysis: M.R.G.; DFT calculations: S.S.; investigation of magnetic properties: K.S.; resources for EDX measurements: J.C.V.; conducting of UV–visible spectroscopy: M.T.; resources for UV–Vis spectroscopy measurements: S.D.; resources for synthesis, impedance and dielectric properties: G.T.; funding acquisition: G.T.; review and editing: M.R.G., G.T.; supervision: G.T. All authors have given approval to the final version of the manuscript.

## Data Availability Statement

The data that support the findings of this study are openly available in ICSD/FIZ at https://icsd.products.fiz-karlsruhe.de, reference number 2309431.

## Keywords

[1] T. Hosaka, T. Shimamura, K. Kubota, S. Komaba, *Chem. Rec.* **2019**, *19*, 735.

[2] Q. Zhang, C. Didier, W. K. Pang, Y. Liu, Z. Wang, S. Li, V. K. Peterson, J. Mao, Z. Guo, *Adv. Energy Mater.* **2019**, *9*, 1900568.

[3] S. Choi, S. Kim, K. Yang, M. Cho, Y. Lee, *ACS Appl. Mater. Interfaces* **2022**, *14*, 17175.

[4] F. Yuan, Y.-C. Shao, B. Wang, Y.-S. We, D. Zhang, Z.-J. Li, Y. A. Wu, *Rare Met.* **2022**, *41*, 3301.

[5] S. Qi, D. Wu, Y. Dong, J. Liao, C. W. Foster, C. O'Dwyer, Y. Feng, C. Liu, J. Ma, *Chem. Eng. J.* **2019**, *370*, 185.

[6] J. Shang, X. Tang, Y. Gu, A. V. Krasheninnikov, S. Picozzi, C. Chen, L. Kou, *ACS Appl. Mater Interfaces* **2021**, *13*, 3033.

[7] A. Fert, *Angew. Chem., Int. Ed.* **2008**, *47*, 5956.

[8] D. B. Gopman, P. Chen, J. W. Lau, A. C. Chavez, G. P. Carmen, P. Finkel, M. Staruch, R. B. Shull, *ACS Appl. Mater. Interfaces* **2018**, *10*, 24725.

[9] C. Wang, C. Chen, C.-H. Chang, H.-S. Tsai, P. Pandey, C. Xu, R. Böttger, D. Chen, Y.-J. Zeng, X. Gao, M. Helm, S. Zhou, *ACS Appl. Mater. Interfaces* **2018**, *10*, 27472.

[10] A. E.-M. A. Mohamed, P. Alvarez-Alonso, B. Hernando, *J. Alloys Compd.* **2021**, *850*, 156713.

[11] M. R. Ghazanfari, A. Santhosh, K. Siemensmeyer, F. Fuß, L. Staab, J. C. Vrijmoed, B. Peters, M. Liesegang, S. Dehnen, O. Oeckler, P. Jerabek, G. Thiele, *Adv. Electron. Mater.* **2022**, *8*, 2200483.

[12] W. Bronger, C. Bomba, *J. Less-Common Met.* **1990**, *158*, 169.

[13] W. Bronger, W. Koelman, D. Schmitz, *Z. Anorg. Allg. Chem.* **1995**, *621*, 405.

[14] W. Bronger, C. Bomba, *J. Less-Common Met.* **1990**, *162*, 309.

[15] W. Li, H. Ding, Z. Li, P. Deng, K. Chang, K. He, S. Ji, L. Wang, X. Ma, J.-P. Hu, X. Chen, Q.-K. Xue, *Phys. Rev. Lett.* **2012**, *109*, 057003.

[16] G. Kresse, M. Marsman, J. Furthmüller, *Vienna Ab Initio Simulation Package (VASP), The Guide*, Universität Wien, Vienna, Austria **2014**.

[17] R. Das, A. Jaiswal, S. Adyanthaya, P. Poddar, *J. Phys. Chem. C* **2010**, *114*, 12104.

[18] G. R. Haripriya, C. M. N. Kumar, R. Pradheesh, L. M. Martinez, C. L. Saiz, S. R. Singamaneni, T. Chatterji, V. Sankaranarayanan, K. Sethupathi, B. Kiefer, H. S. Nair, *Phys. Rev. B* **2019**, *99*, 184411.

[19] K. Binder, A. P. Young, *Rev. Mod. Phys.* **1986**, *58*, 801.

[20] M. Hudl, R. Mathieu, P. Nordblad, *Sci. Rep.* **2016**, *6*, 19964.

[21] E. Maniv, R. A. Murphy, S. C. Haley, S. Doyle, C. John, A. Maniv, S. K. Ramakrishna, Y.-L. Tang, P. Ercius, R. Ramesh, A. P. Reyes, J. R. Long, J. G. Analytis, *Nat. Phys.* **2021**, *17*, 525.

[22] J. Song, Y. Chen, X. Chen, T. Khan, F. Han, J. Zhang, H. Huang, H. Zhang, W. Shi, S. Qi, F. Hu, B. Shen, J. Sun, *Phys. Rev. Appl.* **2020**, *14*, 024062.

[23] J. Juraszek, J. Fassbender, S. Poppe, T. Mewes, B. Hillebrans, D. Engel, A. Kronenberger, A. Ehresmann, H. Schmoranzer, *J. Appl. Phys.* **2002**, *91*, 6896.

[24] P. Zilske, D. Graulich, M. Dunz, M. Meinert, *Appl. Phys. Lett.* **2017**, *110*, 192402.

[25] S. Grimme, J. Antony, S. Ehrlich, S. Krieg, *J. Chem. Phys.* **2010**, *132*, 154104.

[26] G. Kresse, J. Hafner, *J. Phys. Rev. B: Condens. Matter Mater. Phys.* **1993**, *47*, 558.

[27] S. Grimme, S. Ehrlich, L. Goerigk, *J. Comput. Chem.* **2011**, *32*, 1456.

[28] A. A. Kokhanovsky, *J. Phys. D: Appl. Phys.* **2007**, *40*, 2210.

[29] A. K. Bain, P. Chand, in *Ferroelectrics: Principles and Applications*, 1st ed., Wiley-VCH, Weinheim, Germany **2017**, pp. 6–22.

[30] V. Narendar, *Silicon* **2018**, *10*, 2419.

[31] W. Bao, G. N. Li, Q. Z. Huang, G. F. Chen, J. B. He, D. M. Wang, M. A. Green, Y. M. Qiu, J. L. Luo, M. M. Wu, *Chin. Phys. Lett.* **2013**, *30*, 027402.

[32] P. Mishra, P. Kumar, *J. Alloys Compd.* **2012**, *545*, 210.

[33] Z. Osman, M. I. Mohd Ghazali, L. Othman, K. B. Md Isa, *Results Phys.* **2012**, *2*, 1.

[34] H. Yuan, H. Li, T. Zhang, G. Li, T. He, F. Du, S. Feng, *J. Mater. Chem. A* **2018**, *6*, 8413.

[35] M. Duchardt, U. Ruschewitz, S. Adams, S. Dehnen, B. Roling, *Angew. Chem., Int. Ed.* **2018**, *57*, 1351.

[36] E. J. Cheng, M. Liu, Y. Li, T. Abe, K. Kanamura, *J. Power Sources* **2022**, *517*, 230705.

[37] M. R. Ghazanfari, K. Siemensmeyer, A. Santhosh, J. C. Vrijmoed, M. Tallu, S. Dehnen, P. Jerabek, G. Thiele, *Inorg. Chem.* **2023**, *62*, 15358.

[38] B. Hirschorn, M. E. Orazem, B. Tribollet, V. Vivier, I. Frateur, M. Musiani, *Electrochem. Commun.* **2010**, *12*, 1784.

[39] J. Jamnik, J. Maier, *Phys. Chem. Chem. Phys.* **2001**, *3*, 1668.

[40] G. W. Watt, *Chem. Rev.* **1950**, *46*, 289.

[41] O. V. Dolomanov, L. J. Bourhis, R. J. Gildea, J. A. K. Howard, H. Puschmann, *J. Appl. Crystallogr.* **2009**, *42*, 339.

[42] G. M. Sheldrick, *Acta Crystallogr. A* **2015**, *71*, 3.

[43] G. M. Sheldrick, *Acta Crystallogr. C* **2015**, *71*, 3.

[44] K. Brandenburg, *DIAMOND (4.6.4)*, Crystal Impact GbR, Bonn **2020**.

[45] F. Fuß, M. Rieckert, S. Steinhauer, M. Liesegang, G. Thiele, *J. Appl. Crystallogr.* **2022**, *55*, 686.

[46] a) H. M. Rietveld, *Acta Crystallogr.* **1967**, *22*, 151. b) H. M. Rietveld, *J. Appl. Crystallogr.* **1969**, *2*, 65.

[47] B. H. Toby, R. B. von Dreele, *J. Appl. Crystallogr.* **2013**, *46*, 544.

[48] AMETEK Princeton Applied Research DataBase, **2022**, Electrochemical Software, https://www.ameteksi.com/library/application-notes/princeton-applied-research (accessed: November 2022).

[49] P. E. Blöchl, *Phys. Rev. B: Condens. Matter Mater. Phys.* **1994**, *50*, 17953.

[50] G. Kresse, J. Furthmüller, *Comput. Mater. Sci.* **1996**, *6*, 15.

[51] G. Kresse, J. Furthmüller, *Phys. Rev. B: Condens. Matter Mater. Phys.* **1996**, *54*, 11169.

[52] G. Kresse, D. Joubert, *Phys. Rev. B: Condens. Matter Mater. Phys.* **1999**, *59*, 1758.

[53] J. P. Perdew, J. K. Burke, M. Ernzerhof, *Phys. Rev. Lett.* **1996**, *77*, 3865.

[54] W. Setyawan, S. Curtarolo, *Comput. Mater. Sci.* **2010**, *49*, 299.

[55] S. P. Ong, W. D. Richards, A. Jain, G. Hautier, M. Kocher, S. Cholia, D. Gunter, V. L. Chevrier, K. A. Persson, G. Ceder, *Comput. Mater. Sci.* **2013**, *68*, 314.

[56] B. Eck, *wxDragon 2.2.3.*, RWTH Aachen University, Aachen, Germany **2020**.